A superposed epoch investigation of the relation between magnetospheric solar wind driving and substorm dynamics with geosynchronous particle injection signatures

P. D. Boakes,[1,2] S. E. Milan,[1] G. A. Abel,[2] M. P. Freeman,[2] G. Chisham,[2] and B. Hubert[3]

Received 11 August 2010; revised 27 October 2010; accepted 15 November 2010; published 27 January 2011.

[1] We report a superposed epoch analysis of the hemispheric open magnetic flux, maximum nightside auroral intensity, geomagnetic activity, and solar wind and interplanetary magnetic field conditions around the time of substorm onset for three distinct categories of substorms defined by their energetic particle injection signatures. Substorms identified from global auroral imagery are classified into one of three categories based on their energetic particle injection signatures as seen at geosynchronous orbit by the Los Alamos National Laboratory spacecraft. Category 1 events are associated with a "classic" substorm injection, category 2 events show varied activity (i.e., energetic enhancements not following the evolution expected for classic substorms), and category 3 events show no apparent injection activity. The superposed epoch analysis reveals that the three distinct particle injection categories exhibit distinct differences in the level and continuity of magnetospheric driving by the solar wind, such that category 1 events can be described as classic substorm events, category 2 as continuously driven events, and category 3 as weak events. The results of this study suggest that the level and continuity of the dayside solar wind driving of the magnetosphere during substorms have a direct impact on the injection of energetic particles to geosynchronous orbit at substorm onset. These results could have considerable value in empirical predictions of the space weather environment.

Citation: Boakes, P. D., S. E. Milan, G. A. Abel, M. P. Freeman, G. Chisham, and B. Hubert (2011), A superposed epoch investigation of the relation between magnetospheric solar wind driving and substorm dynamics with geosynchronous particle injection signatures, *J. Geophys. Res.*, *116*, A01214, doi:10.1029/2010JA016007.

1. Introduction

[2] Substorms are the fundamental global disturbance of the magnetospheric system. The substorm growth phase is usually defined as a period of 30–60 min of southward oriented interplanetary magnetic field (IMF) [*McPherron et al.*, 1973] during which low-latitude reconnection at the dayside magnetopause opens previously closed terrestrial magnetic field lines to the solar wind. The newly opened magnetic field lines are, subsequently, swept across the polar caps by the solar wind flow [*Dungey*, 1963], leading to the accumulation of open magnetic flux in the magnetotail. The buildup of magnetic energy in the tail cannot continue indefinitely, and it is thought that either a critical threshold within the magnetosphere itself is reached [e.g., *Freeman and Morley*, 2004, 2009] or there is an external trigger in the solar wind [e.g., *Lyons et al.*, 1997], which initiates the onset of explosive magnetic reconnection at a near-Earth neutral line within the magnetotail. Tail reconnection rapidly proceeds onto open magnetic field lines, reclosing large amounts of open magnetic flux during the substorm expansion phase, before slowing during substorm recovery [*Hones*, 1984].

[3] The visible manifestation of the onset of explosive magnetic reconnection in the magnetotail is the global activation of auroral activity [*Akasofu*, 1964]. Typically, the enhanced auroral activity following substorm onset will last for up to an hour, the substorm expansion phase. However, not all nightside auroral brightenings are followed by the global expansion of auroral activity signifying a substorm expansion phase. *Akasofu* [1964] noted that, on occasion, an auroral arc would intensify as if marking the start of substorm onset, but that the auroral activity would fade to background levels after only a few minutes. These events were termed pseudobreakups. It is often hard to distinguish between weak substorms and pseudobreakups, as pseudobreakups can often show one or more signatures of substorm onset [*McPherron et al.*, 2008, and references therein]. *Zhou and Tsurutani* [2001] carried out a statistical study in which substorms, pseudobreakups, and quiescent intervals occurring after interplanetary shocks were associated with strongly southward IMF, near-zero IMF, and strongly northward IMF, respec-

[1]Department of Physics and Astronomy, University of Leicester, Leicester, UK.
[2]British Antarctic Survey, Cambridge, UK.
[3]Laboratory of Planetary and Atmospheric Physics, University of Liège, Liège, Belgium.

0148-0227/11/2010JA016007

tively. *Kullen and Karlsson* [2004] studied 3 months of data containing 419 substorm events and 330 pseudobreakups. They found that large substorms most often occur when the IMF is strongly negative, small substorms most often occur when B_z is weakly positive or 0, and pseudobreakups most often occur for weakly positive B_z and very weak (below average) IMF magnitudes and solar wind density and flow speeds.

[4] Previous studies [e.g., *Craven and Frank*, 1987; *Brittnacher et al.*, 1999; *Milan et al.*, 2003] have shown that the auroral oval, in general, expands to lower latitudes during the substorm growth phase before beginning to rapidly contract at substorm onset. The poleward edge of auroral oval emission is often used as a proxy for the location of the boundary between the more poleward open magnetic field lines and the more equatorward closed magnetic field lines, the open-closed magnetic field line boundary (OCB) [e.g., *Boakes et al.*, 2008, and references therein]. Global hemispheric auroral imagery from orbiting spacecraft, such as the Imager for Magnetopause-to-Aurora Global Exploration (IMAGE) mission [*Mende et al.*, 2000a], thus allows the size of the region enclosed by the auroral oval (the polar cap), and hence the hemispheric open magnetic flux content of the magnetosphere (F_{pc}), to be estimated [e.g., *Milan et al.*, 2003, 2007]. Several studies [e.g., *Milan et al.*, 2003, 2007, 2009a; *Coumans et al.*, 2007; *DeJong et al.*, 2007; *Hubert et al.*, 2008; *Boakes et al.*, 2009; *Huang et al.*, 2009] have employed such methods to show that F_{pc} typically increases by ~25%–35% during the substorm growth phase, while the average F_{pc} at onset is typically between 0.5 and 0.7 GWb (but can be as low as 0.3–0.45 GWb for very weak events and as high as 0.8–1.0 GWb for sawtooth events). These studies also found that F_{pc} typically decreases by ~24%–30% in the substorm expansion phase. Other studies have found that F_{pc} can remain relatively unchanged, or even increase, following substorm onset for events in which the level of dayside reconnection exceeds that on the nightside [e.g., *Coumans et al.*, 2007; *Milan et al.*, 2007].

[5] Another signature of substorm onset is the enhancement of geomagnetic activity as measured by the *AL* and *AU* geomagnetic indices, defined by *Davis and Sugiura* [1966]. During the substorm growth phase, enhanced plasma convection leads to an observed gradual increase in both the *AL* and the *AU* indices [*McPherron*, 1970]. At substorm onset the disruption of the cross-tail current and formation of the substorm electrojet cause a rapid increase in the strength of the *AL* index and subsequent recovery. *Weimer* [1994] carried out a superposed epoch analysis of the *AL* and *AU* indices for 55 substorm events, finding the peak in activity was reached between +25 and +34 min after the time of substorm onset, with the peak in intensity, and subsequent decay, increasing for more intense substorms.

[6] One of the most common signatures used to identify substorms is the injection of energetic electrons and protons into near-Earth orbit [e.g., *Belian et al.*, 1978; *Baker et al.*, 1979]. While various models for the simultaneous acceleration of particles of all energies have been proposed [e.g., *Birn et al.*, 1997; *Sarris and Li*, 2005; *Liu et al.*, 2009; *Asano et al.*, 2010; and references therein], the phenomenological evolution of particle injection at substorm onset is well known [e.g., *McIlwain*, 1974; *Mauk and Meng*, 1983; *Reeves et al.*, 1996]. A spacecraft located within the so-called injection region, located near midnight magnetic local times (MLTs) and spanning several hours of MLT, usually observes a dispersionless enhancement of energetic electrons and protons of all energies. Due to gradient and curvature drift, electrons subsequently drift eastward and protons westward, such that spacecraft located outside of the injection region will observe the energy-dispersed signature of injection. The evolution of particle injection in such a manner is defined as a "typical" or "classic" substorm injection signature. Such injection signatures have been shown to be associated with almost all other signatures of substorm onset [e.g., *Arnoldy and Chan*, 1969; *Belian et al.*, 1981; *Yeoman et al.*, 1994; *Abel et al.*, 2006]. However, *Boakes et al.* [2009] showed that not all substorms identified from global auroral brightenings occur in conjunction with the expected particle injection signature of substorm onset. In a study of 135 events they found that 26% of events could not be associated with any injection activity. They also found that substorms associated with a classic particle injection signature occur, on average, at higher values of F_{pc} at onset than events showing varied or no injection activity. In this paper we investigate this finding further by carrying out a superposed epoch analysis of F_{pc}, auroral intensity, IMF, and solar wind conditions, as well as geomagnetic activity, around the time of substorm onset, for the three particle injection categories defined by *Boakes et al.* [2009].

2. Methodology

[7] In this study we use a subset of substorms identified by *Frey et al.* [2004] from images of the northern hemispheric auroral oval made by the far ultraviolet (FUV) instrument on board the IMAGE spacecraft [*Mende et al.*, 2000a, 2000b]. The FUV instrument consisted of a wideband imaging camera (WIC), and two Spectrographic Imagers, SI12 and SI13. The WIC had a bandwidth of 140–180 nm, observing emissions from the N2 Lyman-Birge-Hopfield band and atomic NI lines. SI12 observed the proton aurora with a pass band of 5 nm centered on the 121.82 nm Doppler-shifted Lyman α. The SI13 detector observed the "excited electron aurora" with a pass band of 5 nm centered on the 135.6 nm OI doublet. The WIC offered the best spatial resolution, ~50 km at apogee, compared to ~100 km offered by both spectrographic imagers. The IMAGE spacecraft was operational from May 2000 to December 2005, when the spacecraft failed. Images were captured at a cadence of 2 min for approximately 10 h of every 14 h orbit. *Frey et al.* [2004] primarily used WIC data, owing to its greater spatial resolution, to identify substorms using the following criteria: (1) a clear local brightening of the auroral oval must be observed, (2) the local brightening must expand to the poleward boundary of the auroral oval and spread azimuthally in local time for at least 20 min, and (3) a substorm onset was accepted as a separate substorm only if at least 30 min had passed since the previous onset. When WIC data were absent, SI13 images were used instead.

[8] The method of *Boakes et al.* [2009] is used to estimate F_{pc} from WIC images of the northern polar cap. In brief, each auroral image is divided into 24 latitudinal profiles, each taken from a longitudinal swath 1 h of MLT wide. The

latitudinal variation of the longitudinally averaged intensity within each profile is fitted by a Gaussian plus quadratic function. Here the Gaussian is expected to fit to the latitudinal profile of the auroral oval, whereas the quadratic fits to any background luminosity. Extra fitting criteria are employed to account for dayglow and double Gaussian auroral oval profiles. The OCB is then assumed to be placed poleward of the center of the most poleward Gaussian fit meeting the fitting criteria by an amount equal to the Gaussian full width at half-maximum (FWHM). *Boakes et al.* [2008] studied the latitudinal difference between the OCB estimated in this manner and that estimated from particle precipitation measurements from the DMSP spacecraft (thought to provide the most direct and precise proxy for the OCB but unable to provide a global proxy owing to its limited spatial resolution). They found systematic offsets between the two methods (see their Figure 5) that are applied to "correct" the WIC OCB estimates. A Fourier expansion is applied to the estimates of OCB latitude, returning a final estimation of the OCB at 48 evenly spaced MLTs. F_{pc} is determined by numerically integrating the radial component of Earth's magnetic field at auroral heights along the 48 latitudinal meridians, each a half-hour of MLT in width, in steps of 0.5° of latitude from the magnetic pole to the latitude of the OCB. *Boakes et al.* [2009] used WIC data from December 2000 and January and December 2001 and 2002 to estimate F_{pc}. Data from December and January months only are used, as the increasing levels of dayglow for other months cause increased uncertainty in identifying the boundaries.

[9] We classify all substorm onsets identified by *Frey et al.* [2004] in the months of December 2000–2002 and January 2001–2002 into three categories based on their particle injection signatures, as defined by *Boakes et al.* [2009]. Low-energy particle summary plots provided by measurements from the Synchronous Orbit Particle Analyzer (SOPA) instruments on board the Los Alamos National Laboratory (LANL) spacecraft [*Belian et al.*, 1992] are used to classify the substorms. The LANL spacecraft are located at geosynchronous orbit, with data from three to four spacecraft typically received simultaneously. Substorms are divided into one of three categories, similar to the categories defined by *Abel et al.* [2006] (examples of which are shown therein): (1) a classical substorm injection signature, (2) unclear activity, and (3) no activity. Substorms falling into category 1 will normally have a clear signature of the simultaneous injection (low dispersion or dispersionless injections) of energetic particles of all energies (electrons were measured in six energy channels between 50 and 500 keV, and protons were measured in five energy channels between 50 and 400 keV by the LANL spacecraft) in the midnight sector, followed by the energy-dispersed signature of simultaneous injection seen by satellites (typically two or more) located at earlier and later MLTs. Events when no satellite data are available in the midnight sector but a dispersed signature is seen by at least three other satellites, consistent with gradient-curvature drift of particles from a dispersionless enhancement near midnight, are also included in this category. Category 2 covers all other energetic particle fluctuations not falling within category 1. Category 3 events show no fluctuations in any of the LANL spacecraft. To be included in this category, data must be available in the midnight sector. Both electron and proton data are used in the classification process. Of the 451 substorms in the Frey onset list for the months used in this study, we are able to classify 306 events into the three LANL categories (that is, 145 onsets are rejected owing to a lack of available LANL spacecraft data), finding relatively even numbers in each: 100 (33%) in category 1, 114 (37%) in category 2, and 92 (30%) in category 3.

[10] Progressing through the plots in Figure 1, we present a superposed epoch analysis of F_{pc} (Figure 1a), the maximum nightside auroral intensity (I) (Figure 1b), IMF components B_x, B_y, and B_z, and their absolute magnitudes (Figures 1c–1h), the solar wind proton density, dynamic pressure, and flow speed (Figures 1i–1k), the SYM-H index (Figure 1l), the Akasofu ε parameter, given by equation (1) here (Figure 1m), and finally, the AU and AL geomagnetic indices (Figure 1n). Category 1 events are shown by the green line, category 2 by the red line, and category 3 by the blue line. The maximum nightside auroral intensity is taken to be the maximum count rate found between 18 and 6 MLT, between 50° and 90° magnetic latitude, and between 0 and 4000 counts in the WIC data. We find that including counts above a threshold of 4000 can introduce large spikes in the superposed epoch traces of mean intensity owing to some very high count rates originating from nonauroral sources in a limited number of images (e.g., from instrumental errors). A threshold of 4000 counts produces a very good match between the mean intensity plot in Figure 1b and a similar plot produced using the median values of intensity in the binning process. Corrected counts are used throughout this study, where corrections for flatfield, gain of the MCP, etc., have been applied so that 1 Rayleigh of emission always produces the same number of counts anywhere in the CCD. One-minute-resolution solar wind and IMF data are provided by the OMNI Definitive, 1 AU 1 min IMF and Plasma database, courtesy of CDAWeb. Plasma and magnetic field data from the ACE [*McComas et al.*, 1998; *Smith et al.*, 1998; *Stone et al.*, 1998], Wind [*Lepping et al.*, 1995; *Ogilvie et al.*, 1995; *Franz et al.*, 2001], and Geotail [*Nishida et al.*, 1992; *Frank et al.*, 1994; *Kokubun et al.*, 1994] spacecraft were used to produce averaged 1 min resolution plasma and IMF data sets shifted to Earth's bow shock nose using a minimal variance technique [see *Weimer et al.*, 2003]. All solar wind data used in this paper are in GSM coordinates. Ground magnetometers provide 1 min resolution AL, AU, and SYM-H indices. The Akasofu ε parameter is an empirically determined fraction of the solar wind Poynting flux through the dayside magnetopause [*Perreault and Akasofu*, 1978] and is thus a measure of the solar wind energy input into the magnetosphere due to dayside reconnection. Here we define the ε parameter as

$$\varepsilon = \frac{V_x B^2}{\mu_0} \sin^4(\theta/2), \tag{1}$$

where B is the total IMF strength ($B = \sqrt{B_x^2 + B_y^2 + B_z^2}$), V_x is the X component of the solar wind flow speed, θ is the IMF clock angle ($\theta = \arctan(|B_y|/B_z)$), and μ_0 is the permeability of free space. This has a functional form similar to that of equations used to estimate the dayside reconnection rate [e.g., *Milan et al.*, 2008], and thus its magnitude also gives an indication of the level of dayside reconnection. Here we have

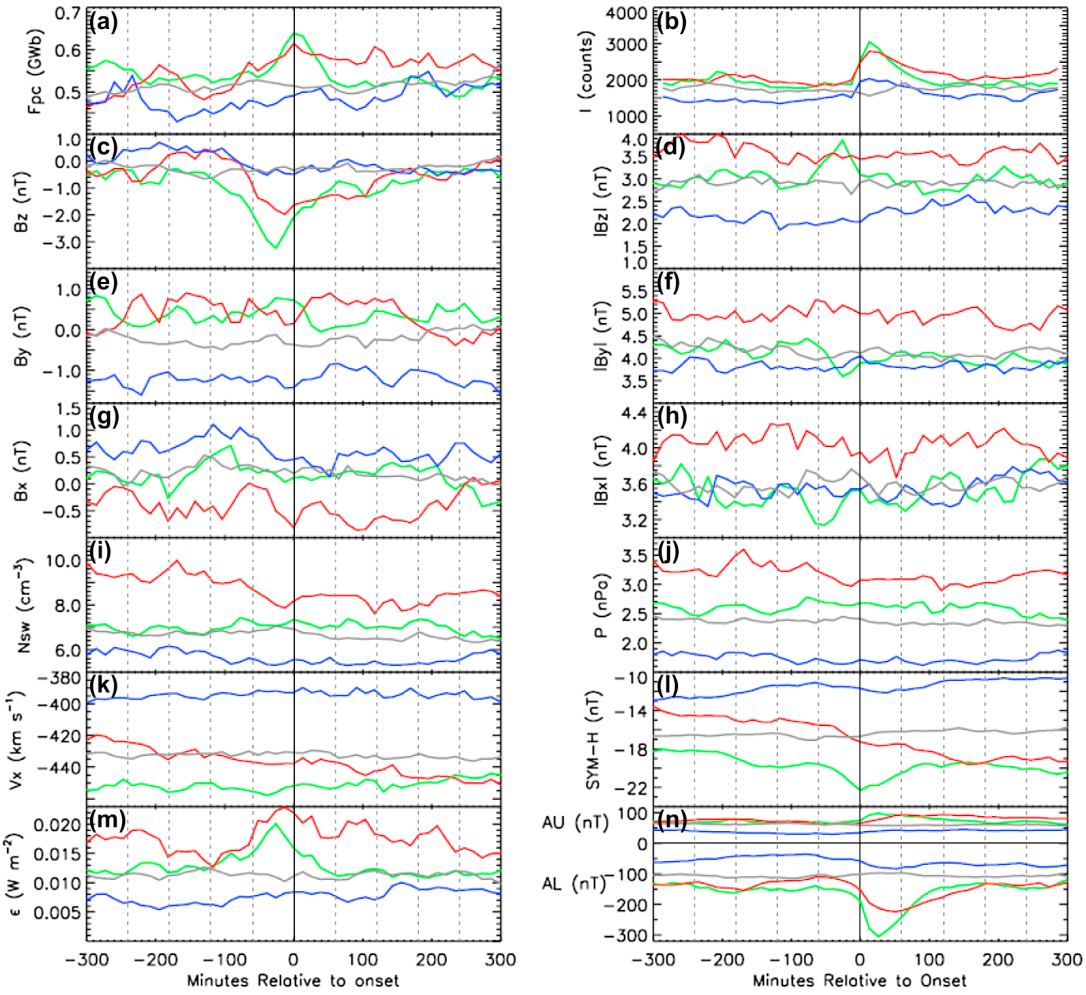

Figure 1. Superposed epoch analysis of (a) open magnetic flux, (b) maximum nightside auroral intensity, (c) interplanetary magnetic field (IMF) B_z, (d) $|B_z|$, (e) IMF B_y, (f) $|B_y|$, (g) IMF B_x, (h) $|B_x|$, (i) solar wind proton number density, (j) solar wind flow pressure, (k) x component of the solar wind flow speed, (l) SYM-H index, (m) Akasofu ε parameter, and (n) AU and AL geomagnetic indices, keyed to the time of substorm onset for the three distinct particle injection categories of substorms. Green represents category 1, red represents category 2, and blue represents category 3. Gray lines represent the average conditions of each parameter for the period of study. The bold vertical line represents the time of substorm onset, and dashed vertical lines show the hours from onset time.

left out the length constant l_0, such that ε has units of power per unit area.

[11] A superposed epoch time series of each parameter relative to the time of substorm onset (shown by the bold vertical line at $t = 0$ in Figures 1a–1n; dashed vertical lines represent hours from onset) is produced using the following procedure: For each Frey onset within the relevant LANL category we find all values of the relevant parameter that lie within ±5 h of the onset time. The data are then placed in bins of 13 min, such that the bin centered on substorm onset contains all values within ±6 min of the onset time. The mean of all values in each 13 min bin and across all substorms within the relevant category is then taken. We find that using the medians in the binning process does not affect any of the superposed traces significantly, but the means provide slightly smother variations in which the main trends are easier to discern. Also overplotted in each panel is a control line (gray) representing the average conditions and variations for the whole period of study, not keyed to substorm onset. This is calculated by adding one IMAGE orbital period (14.2 h) to every LANL category onset epoch, a total of 306 events, before carrying out the same binning procedure as before keyed to this new shifted time for all 306 epochs. We shift the onset times by one IMAGE orbit so as to introduce no biases in the viewing angle of the WIC detector. We note that only two of the shifted control line epochs fall within 30 min of a substorm listed by *Frey et al.* [2004], and only 33 events (11%) fall within 1 h of a Frey et al. onset, giving us confidence that the control lines are not adversely effected by injection events themselves. Using any smoothing methodology produces similar magnitude control lines but eliminates the average control line fluctuations used to analyze the significance of fluctuations in the LANL category superposed traces. Using different time

shifts also produces control lines of similar magnitude and with similar-sized fluctuations.

3. Observations

[12] Initial inspection of Figure 1 shows that category 1 and 2 events occur with similar magnitudes and trends in many of the parameters, while, in contrast, category 3 events appear to be much weaker events in all parameters. Therefore, we first summarize and compare the trends and variations seen in category 1 and 2 events in section 3.1 before addressing the much weaker category 3 events in section 3.2.

3.1. Overview of Category 1 and 2 Events

3.1.1. Open Magnetic Flux and Auroral Intensity

[13] The variation of F_{pc} for categories 1 and 2 is presented by the green and red lines, respectively, in Figure 1a. The main characteristic of the variation in F_{pc} for both categories is an increase prior to onset, the growth phase, and a decrease after onset, the expansion phase. *Boakes et al.* [2009] demonstrated that, on average, category 1 events occur with higher values of F_{pc} at onset compared to either category 2 or 3 events. This is confirmed in Figure 1a, with the category 1 F_{pc} rising to a value of 0.64 GWb at the onset time. F_{pc} varies between 0.46 and 0.64 GWb for the entire period of study, consistent with values found in previous studies [e.g., *Coumans et al.*, 2007; *DeJong et al.*, 2007; *Milan et al.*, 2007; *Huang et al.*, 2009]. Prior to −52 min, F_{pc} remains relatively steady, fluctuating between 0.52 and 0.57 GWb, values slightly higher than the mean of the control line flux (0.51 GWb), representing the average conditions for all events. A rapid increase in F_{pc} is then seen, with F_{pc} rising from a value of 0.53 GWb at −52 min to a value of 0.64 GWb at onset, a percentage increase of ~21%, similar to the percentage increase typically found for substorms [e.g., *Coumans et al.*, 2007]. Following onset, F_{pc} begins to decline immediately, until a value of 0.51 GWb is reached at +78 min, a percentage decrease of ~20%, consistent with the typical F_{pc} decrease observed for both isolated substorms and sawtooth events [e.g., *DeJong et al.*, 2007; *Huang et al.*, 2009]. Thereafter, F_{pc} fluctuates at values similar to the control line flux (gray). The fluctuations in F_{pc} both prior to the F_{pc} growth phase and following the expansion phase are similar in size to the fluctuations seen in the control line, suggesting that they are insignificant.

[14] From the start of the period of study to approximately −120 min, category 2 F_{pc} values fluctuate between 0.46 and 0.56 GWb, similar to the control line flux. At approximately −120 min, F_{pc} begins to increase gradually, the rate of increase accelerating at −91 min, which we take to be the beginning of the F_{pc} growth phase for category 2 events. This growth phase is approximately 30 min longer than the F_{pc} growth phase seen for category 1 events and increases F_{pc} from a value of 0.50 GWb at −91 min to a value of 0.61 GWb at onset, an increase of 22%, similar to the increase for category 1 and typical of substorms. Following onset the decrease in F_{pc} is much less pronounced but more prolonged than for category 1, lasting for approximately 90 min and reducing F_{pc} by ~0.045 GWb. That is, F_{pc} decreases by only 7% in the expansion phase. Following the end of the expansion phase F_{pc} continues to fluctuate between 0.55 and 0.60 GWb for the remainder of the period, comfortably above the control line flux and F_{pc} prior to substorm onset. A smaller secondary peak in F_{pc} appears at approximately −3 h; this is discussed more fully in section 4.3.

[15] The maximum nightside auroral intensity (I) is presented in Figure 1b. Prior to substorm onset both the category 1 (green trace) and the category 2 (red trace) I show little variation and fluctuate at values only slightly elevated from the control line. At onset both the category 1 and the category 2 I increase rapidly. Similar to the behavior of the category 1 F_{pc}, after the peak has been reached, the category 1 I decreases rapidly, returning to control line values at approximately +120 min and thereafter remaining relatively steady for the remainder of the period of study. As with the category 2 F_{pc}, the category 2 I has a more prolonged and less rapid decline, halting at approximately +158 min, whereafter I remains slightly elevated from the category 1 and control line trace for the remainder of the period.

3.1.2. Solar Wind and Interplanetary Magnetic Field Conditions

[16] Category 1 and 2 IMF and solar wind conditions are represented by the green and red lines, respectively, in Figures 1c to 1h. From the beginning of the period of study to approximately −130 min, the category 1 superposed B_z (green trace, Figure 1c) fluctuates between −0.3 and −0.9 nT, similar to the values of the control line (gray trace), which has a mean of 0.0 nT. This is followed by a large and rapid increase in the negative magnitude of B_z, with −3.2 nT being reached at −26 min. Subsequently, B_z sharply turns toward less negative magnitudes, a value of −0.8 nT being reached at approximately +60 min. Thereafter B_z slowly progresses toward less negative values but is always more negative than the control line.

[17] The category 2 superposed B_z is represented by the red trace in Figure 1c. From the start of the period to approximately −200 min the category 2 B_z fluctuates at values similar to that for category 1 before moving to slightly positive values between −180 and −120 min. The B_z begins to increase in negative magnitude at the same time that the negative excursion is seen in category 1 events, the rate of change increasing rapidly at −78 min. The most negative value, about −1.9 nT, is reached at −13 min, approximately 10 min later than for category 1 events. Similar to the trends seen in F_{pc} and I, the recovery of B_z toward control line values is much less rapid than for category 1 events, continuing for up to 3 h after onset.

[18] Figure 1d presents the absolute magnitude of B_z. Category 1 events fluctuate around the control line values for the entire period of study, except for a period of ~2 h starting ~1 h prior to onset, corresponding to the large negative excursion seen in B_z in Figure 1c. In general, the category 2 $|B_z|$ is elevated from both category 1 and the control lines for the entire period of study. B_y, B_x, and their absolute magnitudes are presented in Figures 1e–1h. B_y (Figure 1e) is slightly elevated from the control line for both categories, while the category 2 $|B_y|$ (Figure 1f) is significantly elevated from both the control line and category 1. Both B_x and $|B_x|$ for category 1 (Figures 1g and 1h) fluctuate at values similar to those of the control line, while the $|B_x|$ for category 2 events is elevated from that of category 1 and the control line, with the category 2 B_x fluctuating at negative values. Figures 1i–1k present the superposed solar wind proton density, dynamic

pressure, and V_x component of the solar wind flow speed, respectively. Category 2 events show elevated magnitudes of density and pressure, compared to the control lines or category 1, while category 1 events occur at an elevated flow speed. The superposed IMF and solar wind conditions suggest that while category 1 events occur at average IMF and solar wind conditions, category 2 events occur during more sustained active conditions.

[19] Figure 1m presents the superposed ε parameter, a proxy for the dayside reconnection rate. As expected from the form of equation (1), category 1 ε closely anticorrelates with the variations of the B_z component of the IMF (Figure 1c), with a correlation coefficient of −0.9. From the start of the period of study to approximately −130 min, ε fluctuates around the control line values before rapidly increasing in conjunction with the large negative excursion of B_z. A maximum value is reached at −26 min, the same time that B_z reaches its most negative value. Subsequently, ε drops rapidly until +91 min, after which it remains close to the control line.

[20] As for category 1 events, category 2 events also show a close anticorrelation between IMF B_z and ε, also with a correlation coefficient of −0.9. However, the category 2 ε is elevated from the control line and category 1 ε for the entire period of study. At the beginning of the period of study ε is significantly elevated from the control line and category 1 values, dropping to control line fluxes at approximately −117 min. In conjunction with the negative excursion seen in the category 2 B_z, ε then shows a rapid increase in magnitude. A peak is reached at −13 min, the same time as the negative peak in B_z. As with B_z, ε subsequently declines slowly, always remaining elevated from the control line and category 1 events, for the remainder of the period. The elevated magnitudes of ε for category 2 events following onset suggest that the events of this category are highly influenced by continued dayside reconnection throughout their expansion phases, resulting in the slower decline of F_{pc} and I shown in Figures 1a and 1b.

[21] Here we note that despite the higher level of ε, and inferred increase in the addition of open magnetic flux to the magnetosphere through dayside reconnection, for category 2 events, the peak of the category 1 F_{pc} reaches a slightly higher value than that for category 2. This is evidently a result of the differences between categories seen in the starting level of F_{pc} at the beginning of the study period. At −300 min the F_{pc} of category 1 events is ~0.1 GWb higher than that for category 2. The category 1 F_{pc} and ε thereafter remain relatively steady until approximately −130 min, whereafter they rise in conjunction with an increase in the negative magnitude of the IMF B_z. In contrast, the elevated magnitude of the category 2 ε at the beginning of the period causes an increase in category 2 F_{pc} to values greater than that for category 1. As the IMF B_z component becomes positive at between −180 and −120 min, this is followed by a decrease in the category 2 F_{pc} back to a level below that of category 1. Presumably, this is a result of a drop in the rate of creation of open magnetic flux at the dayside magnetopause, as indicated by the reduction in ε, and the continued closure of flux on the nightside by reconnection at a distant neutral line [*Dungey*, 1963] and/or substorms (see section 4.3). As the IMF B_z component subsequently turns southward at the beginning of the substorm growth phase, ε increases and F_{pc} begins to rise. The observation that the category 2 F_{pc} does not rise as sharply as the category 1 F_{pc}, despite its higher level of dayside reconnection (ε), may suggest that ongoing closure of flux on the nightside of the magnetosphere (nonsubstorm activity) continues at a higher level during the more active periods of category 2 events, compared to category 1.

3.1.3. Geomagnetic Activity

[22] The superposed geomagnetic indices, SYM-H, *AU*, and *AL*, are presented in Figures 1l and 1n, respectively. The category 1 SYM-H (green trace) is found at higher magnitudes than that for category 2 or the control line for the entire period of study. The SYM-H gradually increases in negative magnitude from the beginning of the period of study to approximately −78 min, where a negative bay begins to form. The peak magnitude is reached at the onset time, before gradually declining back to nominal levels (for category 1). The category 2 SYM-H fluctuates at lower magnitudes than that for category 1 and the control line, gradually increasing in magnitude over the entire period of study. The negative enhancement of the SYM-H index for substorm events with larger values of F_{pc} (category 1) is consistent with results of previous superposed studies [*Milan et al.*, 2008, 2009a, 2009b; *Huang et al.*, 2009].

[23] The category 1 *AL* and *AU* indices (Figure 1n, green trace) show the expected bays associated with the onset of substorms. As with the SYM-H index, both the *AL* and the *AU* magnitudes fluctuate at values greater than the control lines for the entire period of study. The peaks in *AL* and *AU* are reached at +26 min. The category 2 *AL* and *AU* also show the expected bay signature of substorms, although the peak magnitudes are reached at the slightly later times of +52 and +65 min and are slightly lower. The recovery of category 2 AL and AU towards control line values after onset occurs more gradually over a longer time period (~3 h) than for category 1 events, similar to F_{pc}, I, B_z, and ε. The peak in the category 1 *AL* and *AU* at +26 min is consistent with the range of 25 to 34 min (peak times for substorms with peak *AL* magnitudes between 600 and 1600 nT and between 400 and 600 nT, respectively) found by *Weimer* [1994]. In contrast, the category 2 *AU* and *AL* magnitudes peak considerably later but may be consistent with the finding that the lower the magnitude of the substorm bay, the longer it takes for the peak to be reached.

3.2. Category 3 Events

[24] The results of *Boakes et al.* [2009] showed that category 3 events occur, on average, at lower values of F_{pc} at onset than either category 1 or category 2 events. This is confirmed by the blue trace in Figure 1a, with an F_{pc} of ~0.49 GWb reached at the onset time. This is below the value of the control line flux at this time and at the lower end of F_{pc} onset values found in previous studies. F_{pc} does not peak at onset, instead rising slowly from approximately −169 min until a peak of 0.51 GWb is reached at +39 min. For the majority of the period F_{pc} remains below the control line flux. The maximum nightside auroral intensity (Figure 1b, blue trace) also remains below the control line for the majority of the 10 h of study, rising above the control line for a period of ~1 h starting around the onset time. The IMF B_z component (Figure 1c) and $|B_z|$ (Figure 1d) fluctuate at values lower than or comparable to those of the control lines. The B_y (Figure 1e) and $|B_y|$ (Figure 1f) components of

the IMF are also found at smaller magnitudes than the control lines and other categories. The B_y component is shifted toward negative values, fluctuating between approximately −1.6 and −0.8 nT for the entire period, suggesting that category 3 events occur during negative B_y conditions. The B_x component (Figure 1g) is found at slightly more positive values than the control line, as may be expected to accompany a negative B_y shift due to anticorrelation between B_x and B_y in the Parker spiral. This is almost the opposite of what is seen for category 2 events, suggesting that category 2 and 3 events occur in different sectors of the Parker spiral (i.e., above or below the heliospheric current sheet). The category 3 solar wind proton density (Figure 1i), pressure (Figure 1j), and flow speed (Figure 1k) are all significantly reduced compared to those for category 1 and 2 events and the average control lines. Similarly the SYM-H, *AL*, and *AU* indices also fluctuate at values below those of the control lines and are significantly reduced in magnitude compared to those of category 1 and 2 events, suggesting that category 3 events occur during very quiet geomagnetic conditions. Minimal disturbances are seen in the *AL* and *AU* indices at the time of onset for category 3 events. The substorms used in this paper are from the Northern Hemisphere winter solstice. During this time the LANL spacecraft can be displaced significantly from the magnetic equator such that any spacecraft with a significant displacement may be located outside of the region of any weak particle enhancements. We investigated this displacement, to determine whether the lack of particle enhancement for any category 3 events could be explained in this manner, and found seven category 3 events for which the LANL spacecraft located near midnight were found to be significantly displaced from the equator and thus may miss weak injections. However, the selection criterion for categorization requires that data from at least three LANL spacecraft, well spread in MLT, must be available. We find that the spacecraft located at earlier and later MLTs for the seven events mentioned are found very close to the magnetic equator and therefore may be expected to see the drift signature of even weak substorm injections. Thus, the lack of injection signature for category 3 events cannot be explained by spacecraft location, and since we find no biases in LANL spacecraft location (in MLT or magnetic latitude) between categories, we conclude that spacecraft location does not define the differences seen between them.

4. Summary and Discussion

[25] To have confidence in any conclusions drawn from this study it is important to discuss the statistical significance of the trends and variations seen in the superposed plots. The standard errors of all parameters, and for all categories, in Figure 1 are comparable in size to the smallest of the fluctuations seen in any of the parameters, and much smaller than any significant fluctuations considered. A very small number of events in each category are found to occur during stronger than average solar wind conditions. However, removing these events from the analysis reveals that they do not affect the variations presented in Figure 1. We conclude that the variations and trends seen are true representations of the differing LANL categories.

4.1. Summary of Trends and Variations

[26] Here let us summarize the main findings of section 3 before discussing the role of solar wind triggering (section 4.2), substorm periodicity (section 4.3), and the level of solar wind driving (section 4.4) in defining the properties of the LANL categories. Category 1 events (represented by green traces in Figure 1) are defined by their "classical" particle injection signatures and show all the expected signatures of classically defined substorms in all parameters. This includes clear substorm growth and expansion phases in F_{pc} (Figure 1a) and *AL* and *AU* indices (Figure 1n), a rapid brightening of the nightside auroral intensity at substorm onset (Figure 1b), and a classic substorm growth phase in IMF B_z (i.e., strong and southward IMF for up to an hour prior to onset; Figure 1c). They are the largest and most energetic of the three categories, with the largest magnitudes reached in F_{pc}, *I*, and geomagnetic indices; Figures 1l and 1n). F_{pc} increases by ~21% in the F_{pc} growth phase and decreases by ~20% following onset, consistent with the values found in previous studies of "classical" substorm or sawtooth events [e.g., *Caan et al.*, 1978; *McPherron and Hsu*, 2002; *Huang et al.*, 2009]. They occur in periods of enhanced geomagnetic activity (*AL*, *AU*, and SYM-H; Figures 1l and 1n) but average IMF and solar wind conditions (IMF B_z, B_y, B_x, proton density, and pressure; Figures 1c–1h), although with slightly elevated solar wind flow speeds (Figure 1k).

[27] Category 2 events are defined as events that show any energetic particle enhancements at geosynchronous orbit that do not follow the classical definition of substorm injections and are represented by the red traces in Figure 1. Category 2 events show several characteristics of substorm onset, including a southward turning of the IMF B_z (Figure 1c), an ~22% increase in the F_{pc} growth phase (Figure 1a), geomagnetic bays in *AL* and *AU* indices (Figure 1n) and a rapid brightening of the nightside auroral oval (Figure 1b). They generally occur during periods of enhanced IMF and solar wind conditions (proton density, pressure, and IMF magnitudes; Figures 1i, 1j, and 1c–1h, respectively) but lower geomagnetic activity (Figures 1l and 1n). The defining characteristic of category 2 events is the continued elevation of parameters following onset, for example, in F_{pc} (Figure 1a), *I* (Figure 1b), *AL* and *AU* indices (Figure 1n), and ε (Figure 1m).

[28] Category 3 events are defined by their lack of particle injection signatures and are represented by the blue traces in Figure 1. Category 3 events do not show typical substorm growth and expansion phases in any of the parameters studied. F_{pc} rises slowly from well before the onset time and continues to do so up to +50 min after onset (Figure 1a), remaining below the control line flux for the majority of the period of study. There is no large southward turning of the IMF B_z indicative of substorm growth phases. A small increase, and subsequent slow decline, is seen in the maximum nightside auroral intensity (Figure 1b). This is evidently the auroral brightening indentified as substorm onset. Very small scale geomagnetic disturbances are also seen in *AL* (<100 nT) and *AU* (<50 nT) indices (Figure 1n), although these are below the average activity as represented by the control lines (gray). Pseudobreakups are known to be associated with small geomagnetic bays, less than 100 nT [e.g., *Koskinen et al.*, 1993], suggesting that pseudobreakups

may be included, along with weak substorms, in this category. They also occur during quiet geomagnetic conditions (*AL*, *AU*, and SYM-H; Figures 1l and 1n), weak solar wind flow (Figures 1c–1k), and weakly negative or positive IMF B_z, consistent with weak substorm events [e.g., *Zhou and Tsurutani*, 2001; *Kullen and Karlsson*, 2004]. The average IMF B_y component (Figure 1e) is shifted toward negative values, which is unexpected. The negative B_y is accompanied by a positive B_x, as may be expected from the anticorrelation of B_x and B_y in the Parker spiral. This is opposite to what is seen for category 2 events, suggesting that category 2 and 3 events occur when Earth is subject to different sectors of the Parker spiral (above or below the heliospheric current sheet). Investigation of the B_y distributions for the 5 months of data used in this study reveals that, for all months bar one, B_y is relatively evenly distributed around 0 nT. All distributions except that of January 2002 having absolute means of <0.61 nT. The distribution of B_y in the month of January 2002, however, exhibits a significant negative peak, shifting the mean to negative values (−1.12 nT). Category 1 and 2 events are relatively evenly spread throughout the 5 months used in this study. However, we find that 38% (35 events) of category 3 onsets occur during the negative B_y month of January 2002. This is significantly greater than the percentage we would expect from the null hypothesis that B_y has no effect on category 3 events (in which case we would expect the category 3 substorms to be evenly spread throughout the 5 months such that 20% of the events would be found in January 2002), but we cannot think of any reason why weak substorms should be associated with negative B_y, and the bias seen may be a result of a bias in the data set used in this study, and not a characteristic of substorm events showing no particle injection signatures. The real association for category 3 events may be periods in which $|B_y|$ is elevated compared to $|B_z|$, such that the category 3 IMF clock angle is closer to 90°, contributing to the much weaker solar wind input for these events compared to category 1 and 2 events. Indeed, the mean of the category 3 $|B_y|$ component in the hour prior to onset is elevated from the mean of the category 3 $|B_z|$ component by ~1.9 nT, compared to an elevation of 1.6 nT for category 2 events and ~0.4 nT for category 1 events.

4.2. Solar Wind Triggering

[29] The large decrease in the negative magnitude of the category 1 B_z component in the half-hour preceding substorm onset may lead some observers to suggest that these events could be triggered by a northward turning of the IMF. Conversely, the more gradual change in B_z for category 2 events may lead some to suggest that these events are nontriggered events. *Morley and Freeman* [2007] developed an automated technique to identify northward triggers using the quantitative rules defined by *Lyons et al.* [1997] (see *Morley and Freeman* [2007] for the list of criteria used in identifying a northward turning). Using a similar method, we find that 44% of category 1 events, 29% of category 2 events, and 17% of category 3 events can be associated with a northward turning. If northward turnings do trigger events in our data set, it is clear that category 1 does not hold exclusivity on these events. It is more likely that the increased number of "triggered" events in this category and the large northward turning seen in the superposed trace of B_z are a consequence of the form of the growth phase and solar wind driving (see section 4.4) of these events, rather than an indication that they are triggered. That is, substorms require a period of southward IMF prior to onset (the substorm growth phase), seen as a large negative excursion in the superposed B_z of category 1 and 2 events. Following onset there is no requirement that the IMF be southward, such that the category 1 superposed B_z rapidly returns to fluctuating around its average value of ~0 nT. However, a key characteristic of category 2 events appears to be the continuation of southward IMF into the expansion phase of these events (see below), resulting in a slower decline of B_z back to the average values [see also *Freeman and Morley*, 2009]. *Coumans et al.* [2007] suggested that northward triggered events occur at lower values of F_{pc} than nontriggered events such that, if category 1 events were triggered by the solar wind, they would occur at lower values of F_{pc} than category 2 events, which is the opposite of what is seen in the present study.

4.3. Substorm Periodicity

[30] Initial inspection of Figure 1a suggests that a secondary peak is reached in the category 2 F_{pc} at approximately −3 h, with smaller fluctuations occurring after onset at approximately +2, +3, and +4 h. *Borovsky et al.* [1993] studied the waiting time between substorms identified from particle injection events. They found an average waiting time of ~2.75 h for substorms occurring cyclically and a "random" waiting time of ~5 h for events occurring outside of these intervals. An interesting question that then arises is whether category 2 events are periodic events, occurring with a waiting time similar to the mean waiting time found between periodic substorms, and whether category 1 events are more isolated, occurring with a waiting time more similar to the waiting time found between isolated "random" substorm events. Using the Frey list of substorm onsets, we find that there is little difference between the periodicity of events between categories. In fact, only ~50% of the onsets in either category 1 or category 2 is found to have another substorm within +5 or −5 h, decreasing to 36% for category 3. We conclude that there is no difference in the substorm periodicity for category 1 and 2 events. By visual inspection of the LANL data, we also find fewer than five events in any one category that fall during possible sawtooth periods, and hence we may also draw the conclusion that sawtooth events do not define any of the three categories. Similarly, by visual inspection of the FUV auroral images, we also find that Poleward Boundary Intensifications, transient intensifications observed at the poleward edge of the auroral oval [e.g., *Lyons et al.*, 2002; *Zesta et al.*, 2002], do not determine the properties of the LANL categories.

4.4. Solar Wind Driving

[31] We have shown that substorm periodicity and triggering do not define the trends and variations shown in Figure 1. However, the superposed epoch traces of each parameter appear to be well ordered by the magnitude of the dayside reconnection rate, as inferred from the Akasofu ε parameter (Figure 1m).

[32] As already discussed, the trends and variations shown in Figure 1 suggest that category 1 events (green lines) follow the expected evolution of classically defined substorms. That is, the substorm growth phase is defined by a southward turning of the IMF B_z component (Figure 1c).

This allows magnetic reconnection to occur at the low-latitude dayside magnetopause, seen as a rapid increase in the magnitude of the dayside reconnection rate (ε Figure 1m). The enhanced dayside reconnection opens previously closed terrestrial magnetic flux to the polar caps, seen as a rapid increase in F_{pc} (Figure 1a). Following the substorm growth phase the IMF is no longer required to be southward and B_z begins to recover and fluctuate around nominal values. The onset of explosive reconnection in the magnetotail at substorm onset results in the rapid closure of open magnetic flux. Combined with the return of the dayside reconnection rate to lower magnitudes, this results in a rapid decrease in the total open magnetic flux content of the magnetosphere (F_{pc}; Figure 1a). The defining characteristic of category 2 events (red lines; Figure 1), however, is the continued elevated magnitudes of dayside reconnection following substorm onset (Figure 1m). That is, dayside reconnection continues to add open magnetic flux to the polar cap at an elevated rate, balancing the flux closed by nightside reconnection and resulting in only a 7% decrease in F_{pc} (Figure 1a). The continued driving of the magnetosphere by dayside reconnection for these events is also evident in the slower decline of auroral intensity and geomagnetic activity back to nominal levels. At the other end of the spectrum, category 3 events occur during very weak conditions in all parameters. The ε parameter (blue trace; Figure 1m) indicates that very little dayside reconnection is ongoing, such that we may expect even a relatively small substorm to decrease F_{pc}, which is not seen. This may suggest that nightside reconnection does not progress to open magnetic field lines for this category.

[33] The ε parameter is a function of the solar wind flow speed (V_x), IMF clock angle, and absolute magnitude of the IMF. The variation of the ε parameter closely mirrors that of the IMF B_z component for both category 1 and category 2, suggesting that the IMF B_z is highly influential on the level of dayside reconnection for both events. However, in the hour prior to onset the mean of the category 2 $|B_y|$ (5.11 nT) is significantly elevated from that of the $|B_z|$ (3.49 nT), while for category 1 events the absolute magnitudes are very similar (3.84 nT for B_y and 3.48 nT for B_z). While the IMF B_z component appears to be the controlling factor in the level of dayside driving for category 1 events, the B_y component of the field appears to play a more significant role for category 2.

[34] The LANL energetic particle data show that many category 2 events occur during periods of very active and complicated energetic particle fluctuations. This includes enhancements related to solar wind pressure pulses [e.g., *Lee et al.*, 2005], drift echoes from previous substorms, and large flux dropouts as the spacecraft leave the plasma sheet. This increased magnetospheric activity is likely a result of the more active solar wind conditions and the elevated magnitude and continuation of dayside solar wind magnetospheric driving seen for these events, compared to other categories. *Milan et al.* [2006] carried out a multi-instrument study of a substorm interval occurring during a period of continued southward IMF and, hence, inferred continuous dayside driving. They found that following the second substorm event in their study, the F_{pc} remained elevated for the remainder of the substorm interval and that the maximum nightside auroral intensity, after showing a rapid brightening around the onset time, declined slowly over the next 2.5 h, much like that seen for category 2. Using magnetic field data from spacecraft located in the magnetotail, the authors suggest that the tail dynamics during the substorm is strongly driven by the ongoing dayside creation of open magnetic flux. We suggest that category 2 events are similar to the event in this study in that the tail dynamics and magnetospheric activity are greatly influenced not only by the continued creation of open magnetic flux on the dayside during the substorm expansion phase, but also by the elevated magnitude of the dayside reconnection rate (ε) during their slightly prolonged growth phase, compared to other categories. This also suggests that the directly driven process (in which solar wind energy is directly dissipated into the ionosphere and ring current) plays the dominant role in the driving and control of the tail dynamics and particle injection activity of category 2 events. Category 1 events, in contrast, are more influenced by the loading-unloading process (in which solar wind energy is first stored in the magnetosphere during the substorm growth phase before subsequently being released during substorm expansion). The increased activity and continuous driving for category 2 events may result in the more active conditions seen in the LANL energetic particle data. This increase in activity can complicate or hide any "classic" substorm injection evolution, making it difficult to discern true substorm injection activity from non-substorm-like behavior. It is unclear whether the varied injection activity seen for category 2 events is due to modification of the classic injection signature due to more active tail dynamics and directly driven magnetosphere, whether the substorm injection is hidden or complicated by other nonsubstorm particle activity, or indeed whether the auroral brightenings identified as substorm onset are caused by this nonsubstorm activity itself and are not true global substorms, or, perhaps more likely, a combination of all of these. A more detailed study of the tail dynamics during these events may reveal the true nature of these events. However, the results presented here suggest that the level and continuity of dayside solar wind driving of the magnetosphere have a direct influence on the particle injection signature seen at geosynchronous orbit during substorms.

[35] Category 3 events do not show the expected signatures of global substorm onset events in many of the parameters studied and only very weak signatures of substorm and nightside reconnection activity in auroral intensity and *AU* and *AL* indices compared to category 1 and 2 events, suggesting that they are very weak nightside reconnection events. *Miyashita et al.* [2004] used observations of the tail magnetic field variations during substorms to show that the initial reconnection site of intense substorms (i.e., category 1) tends to be located closer to Earth than that of weaker events (i.e., category 3). *Nagai et al.* [2005] also showed that substorms occurring with stronger or more efficient solar wind energy input (i.e., category 1/2) have their onset location closer to Earth than those with weaker driving (i.e., category 3). The size of the energetic particle injection seen at geosynchronous orbit (and at any fixed observing position) is due to a combination of the particle acceleration (which moves the relatively higher fluxes of low-energy particles to higher energies) and particle transport (which determines whether these higher fluxes of high-energy particles encounter the observer). The particle acceleration is by the inductive electric field associated with the magnetic field dipolarization at substorm onset and, hence, will likely be larger for tail magnetic fields that are more stretched (nondipolar) prior to

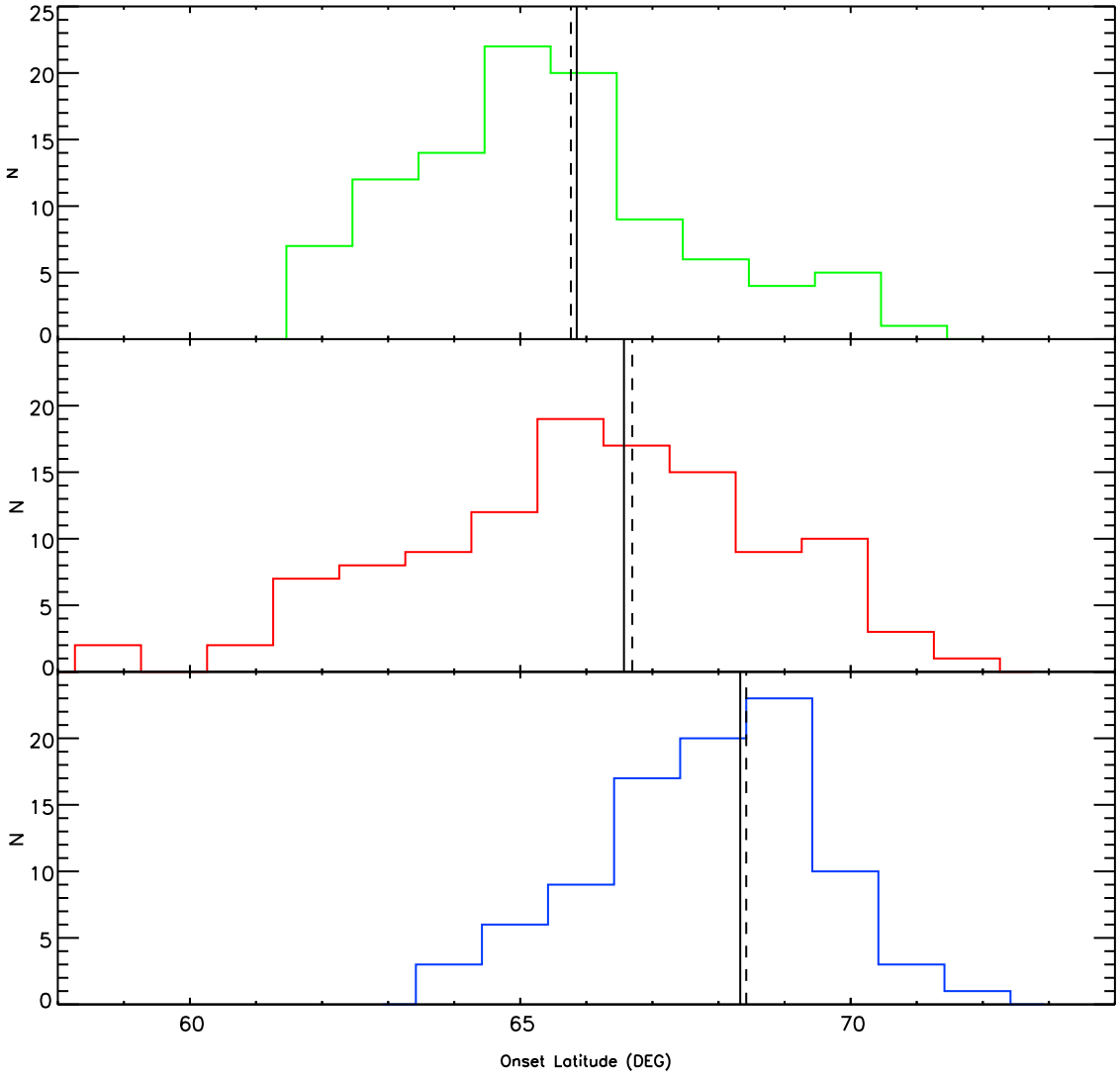

Figure 2. Distributions of onset latitude for the three particle injection categories of substorms. Green represents category 1, red represents category 2, and blue represents category 3. Solid and dashed vertical lines represent the mean and medians of the distribution, respectively.

onset. The transport is a combination of (noninductive) $E \times B$ convection and gradient-curvature drift, and so will likely not bring particles energized in the tail by dipolarization into geosynchronous orbit if the $E \times B$ convection toward Earth is weak compared to the mainly azimuthal gradient-curvature drift. Thus the weak category 3 injections, compared to categories 1 and 2, can be explained by the weaker solar wind input for these events, which causes (a) the tail field to be less stretched at onset and, hence, the particle energization from the field dipolarization to be weaker and (b) the stretched field line region (and hence the reconnection X line) to be farther downtail and the $E \times B$ convection to be weaker, such that any energized particles from (a) will mostly not encounter geosynchronous orbit. Figure 2 presents the distributions of the initial onset latitude of the auroral brightening indentified as substorm onset by *Frey et al.* [2004] for the three LANL categories. The mean and median of onset latitudes for each category are shown by the vertical solid and dashed lines, respectively. Although, in general, onsets from all categories cover approximately the same latitudinal range, a greater proportion of category 3 events occurs at higher latitudes compared to either category 1 or category 2, suggesting that the onset region is indeed located farther from Earth for category 3 events.

5. Conclusions

[36] We have carried out a superposed epoch analysis of the hemispheric open magnetic flux content of the magnetosphere, maximum nightside auroral intensity, geomagnetic activity, and solar wind and IMF conditions around the time of substorm onset for three distinct categories of substorms defined by their particle injection signatures as seen at geosynchronous orbit by the LANL spacecraft. Substorms identified from global auroral imagery have been divided into those associated with a "classic" particle injection signature of substorm onset (category 1), those that showed all other particle enhancements not following this classical evolution (category 2), and those events that we could not associate with any significant particle enhancement (category 3). Of a total

of 451 substorm events identified from global auroral imagery in the months of December and January 2000–2002 by *Frey et al.* [2004], we are able to classify 306 events into the three LANL categories, finding relatively even numbers in each: 100 (33%) in category 1, 114 (37%) in category 2, and 92 (30%) in category 3. We summarize our findings of the superposed epoch analysis as follows.

[37] 1. Category 1 events show all the expected signatures of classic substorm onsets, occurring owing to a large southward turning of the IMF B_z component in the substorm growth phase during otherwise average IMF and solar wind conditions.

[38] 2. Category 2 events appear to occur when the magnetosphere is continuously driven by dayside reconnection throughout the substorm growth and expansion phases, observed as the continued elevation of the negative magnitude of the IMF B_z component and Akasofu ε parameter during substorm expansion, as well as the slow decline of open magnetic flux, auroral intensity, and geomagnetic activity back to presubstorm magnitudes. The magnitude of the IMF B_y component is also enhanced, compared to other categories and the IMF B_z, suggesting that the IMF B_y component may play a more important role in the dayside reconnection for these events. They also generally occur during more active solar wind and IMF conditions.

[39] 3. Category 3 events occur during much weaker solar wind, IMF, and geomagnetic conditions than either category 1 or category 2. They appear to be very weak substorm events or pseudobreakups.

[40] The results of this study suggest that the level and continuity of the dayside solar wind driving of the magnetosphere during substorms has a direct influence on the injection of energetic particles to geosynchronous orbit at substorm onset. Future investigation of the magnetotail magnetic field conditions and plasma sheet evolution for the three distinct particle injection categories may provide important insights into the substorm injection process and its relation to solar wind driving and magnetospheric dynamics. The results presented in this paper, and future work, may have considerable value for studies of space weather, in particular, empirical predictions and models of the near-Earth space environment.

[41] **Acknowledgments.** P.D.B. was supported by a PPARC/STFC CASE award, grant PPA/S/C/2006/04488; S.E.M. was supported by STFC grant PP/E000983/1; B.H. is supported by the Belgian National Fund for Scientific Research (FNRS); G.C. and M.P.F. are supported by the UK Natural Environment Research Council through the Complexity work package of the BAS Environmental Change and Evolution program. The authors would like to thank the many dedicated scientists who have made the IMAGE mission a success. The solar wind data used in this paper were accessed through CDAWeb. *AL*, *AU*, and SYM-H indices were provided courtesy of the World Data Center for Geomagnetism, Kyoto University. We thank H. U. Frey for use of his substorm onset list. We acknowledge the U.S. Department of Energy for the use of the Los Alamos geosynchronous energetic particle data.

[42] Masaki Fujimoto thanks the reviewers for their assistance in evaluating this paper.

References

Abel, G. A., M. P. Freeman, A. J. Smith, and G. D. Reeves (2006), Association of substorm chorus events with drift echoes, *J. Geophys. Res.*, *111*, A11220, doi:10.1029/2006JA011860.

Akasofu, S. I. (1964), The development of the auroral substorm, *Planet. Space Sci.*, *12*, 273, doi:10.1016/0032-0633(64)90151-5.

Arnoldy, R. L., and K. W. Chan (1969), Particle substorms observed at the geostationary orbit, *J. Geophys. Res.*, *74*, 5019–5028, doi:10.1029/JA074i021p05019.

Asano, Y. I., et al. (2010), Electron acceleration signatures in the magnetotail associated with substorms, *J. Geophys. Res.*, *115*, A05215, doi:10.1029/2009JA014587.

Baker, D. N., R. D. Belian, P. R. Higbie, and E. W. Hones (1979), High-energy magnetospheric protons and their dependence on geomagnetic and interplanetary conditions, *J. Geophys. Res.*, *84*, 7138–7154, doi:10.1029/JA084iA12p07138.

Belian, R. D., D. N. Baker, P. R. Higbie, and E. W. Hones (1978), High-resolution energetic particle measurements at 6.6 R sub E: II. High-energy proton drift echoes. III. Low-energy electron anisotropies and short-term substorm predictions, *J. Geophys. Res.*, *83*, 4857–4862, doi:10.1029/JA083iA10p04857.

Belian, R. D., D. N. Baker, E. W. Hones, P. R. Higbie, S. J. Bame, and J. R. Asbridge (1981), Timing of energetic proton enhancements relative to magnetospheric substorm activity and its implication for substorm theories, *J. Geophys. Res.*, *86*, 1415–1421, doi:10.1029/JA086iA03p01415.

Belian, R. D., G. R. Gisler, T. Cayton, and R. Christensen (1992), High-*Z* energetic particles at geosynchronous orbit during the great solar proton event series of October 1989, *J. Geophys. Res.*, *97*, 16,897–16,906, doi:10.1029/92JA01139.

Birn, J., M. F. Thomsen, J. E. Borovsky, G. D. Reeves, D. J. McComas, and R. D. Belian (1997), Characteristic plasma properties during dispersionless substorm injections at geosynchronous orbit, *J. Geophys. Res.*, *102*, 2309–2324, doi:10.1029/96JA02870.

Boakes, P. D., S. E. Milan, G. A. Abel, M. P. Freeman, G. Chisham, B. Hubert, and T. Sotirelis (2008), On the use of IMAGE FUV for estimating the latitude of the open/closed magnetic field line boundary in the ionosphere, *Ann. Geophys.*, *26*, 2759–2769.

Boakes, P. D., S. E. Milan, G. A. Abel, M. P. Freeman, G. Chisham, and B. Hubert (2009), A statistical study of the open magnetic flux content of the magnetosphere at the time of substorm onset, *Geophys. Res. Lett.*, *36*, L04105, doi:10.1029/2008GL037059.

Borovsky, J. E., R. J. Nemzek, and R. D. Belian (1993), The occurrence rate of magnetospheric-substorm onsets—Random and periodic substorms, *J. Geophys. Res.*, *98*, 3807–3813, doi:10.1029/92JA02556.

Brittnacher, M., M. Fillingim, G. Parks, G. Germany, and J. Spann (1999), Polar cap area and boundary motion during substorms, *J. Geophys. Res.*, *104*, 12,251–12,262, doi:10.1029/1998JA900097.

Caan, M. N., R. L. Mcpherron, and C. T. Russell (1978), The statistical magnetic signature of magnetospheric substorms, *Planet. Space Sci.*, *26*, 269–279, doi:10.1016/0032-0633(78)90092-2.

Coumans, V., C. Blockx, J. C. Gerard, B. Hubert, and M. Connors (2007), Global morphology of substorm growth phases observed by the IMAGE-SI12 imager, *J. Geophys. Res.*, *112*, A11211, doi:10.1029/2007JA012329.

Craven, J. D., and L. A. Frank (1987), Latitudinal motions of the aurora during substorms, *J. Geophys. Res.*, *92*, 4565–4573, doi:10.1029/JA092iA05p04565.

Davis, T., and M. Sugiura (1966), Auroral electrojet index AE and its universal time variations, *J. Geophys. Res.*, *71*, 785–801.

DeJong, A. D., X. Cai, R. C. Clauer, and J. F. Spann (2007), Aurora and open magnetic flux during isolated substorms, sawteeth, and SMC events, *Ann. Geophys.*, *25*, 1865–1876.

Dungey, J. W. (1963), The structure of the exosphere or adventures in velocity space, in *Geophysics, The Earth's Environment*, edited by C. Witt, J. Hiebolt, and L. Le Beau, p. 503, Gordon and Breach, New York.

Frank, L. A., K. L. Ackerson, W. R. Paterson, J. A. Lee, M. R. English, and G. L. Pickett (1994), The Comprehensive Plasma Instrumentation (Cpi) for the Geotail spacecraft, *J. Geomagn. Geoelectr.*, *46*, 23–37.

Franz, H., P. Sharer, K. Ogilvie, and M. Desch (2001), Wind nominal mission performance and extended mission design, *J. Astronaut. Sci.*, *49*, 145–167.

Freeman, M. P., and S. K. Morley (2004), A minimal substorm model that explains the observed statistical distribution of times between substorms, *Geophys. Res. Lett.*, *31*, L12807, doi:10.1029/2004GL019989.

Freeman, M. P., and S. K. Morley (2009), No evidence for externally triggered substorms based on superposed epoch analysis of IMF B_z, *Geophys. Res. Lett.*, *36*, L21101, doi:10.1029/2009GL040621.

Frey, H. U., S. B. Mende, V. Angelopoulos, and E. F. Donovan (2004), Substorm onset observations by IMAGE-FUV, *J. Geophys. Res.*, *109*, A10304, doi:10.1029/2004JA010607.

Hones, E. W., Jr. (1984), Plasma sheet behaviour during substorms, in *Magnetic Reconnection in Space and Laboratory Plasmas*, *Geophys. Monogr. Ser.*, vol. 30, edited by E. W. Hones Jr., p. 178, AGU, Washington, D. C.

Huang, C. S., A. D. DeJong, and X. Cai (2009), Magnetic flux in the magnetotail and polar cap during sawteeth, isolated substorms, and steady magnetospheric convection events, *J. Geophys. Res.*, *114*, A07202, doi:10.1029/2009JA014232.

Hubert, B., S. E. Milan, A. Grocott, S. W. H. Cowley, and J. C. Gerard (2008), Open magnetic flux and magnetic flux closure during sawtooth events, *Geophys. Res. Lett.*, *35*, L23301, doi:10.1029/2008GL036374.

Kokubun, S., T. Yamamoto, M. H. Acuna, K. Hayashi, K. Shiokawa, and H. Kawano (1994), The Geotail Magnetic-Field Experiment, *J. Geomagn. Geoelectr.*, *46*, 7–21.

Koskinen, H. E. J., R. E. Lopez, R. J. Pellinen, T. I. Pulkkinen, D. N. Baker, and T. Bosinger (1993), Pseudobreakup and substorm growth phase in the ionosphere and magnetosphere, *J. Geophys. Res.*, *98*, 5801–5813, doi:10.1029/92JA02482.

Kullen, A., and T. Karlsson (2004), On the relation between solar wind, pseudobreakups, and substorms, *J. Geophys. Res.*, *109*, A12218, doi:10.1029/2004JA010488.

Lee, D. Y., L. R. Lyons, and G. D. Reeves (2005), Comparison of geosynchronous energetic particle flux responses to solar wind dynamic pressure enhancements and substorms, *J. Geophys. Res.*, *110*, A09213, doi:10.1029/2005JA011091.

Lepping, R. P., et al. (1995), The Wind Magnetic-Field Investigation, *Space Sci. Rev.*, *71*, 207–229, doi:10.1007/BF00751330.

Liu, W. L., X. Li, T. Sarris, C. Cully, R. Ergun, V. Angelopoulos, D. Larson, A. Keiling, K. H. Glassmeier, and H. U. Auster (2009), Observation and modeling of the injection observed by THEMIS and LANL satellites during the 23 March 2007 substorm event, *J. Geophys. Res.*, *114*, A00C18, doi:10.1029/2008JA013498.

Lyons, L. R., G. T. Blanchard, J. C. Samson, R. P. Lepping, T. Yamamoto, and T. Moretto (1997), Coordinated observations demonstrating external substorm triggering, *J. Geophys. Res.*, *102*, 27,039–27,051, doi:10.1029/97JA02639.

Lyons, L. R., E. Zesta, Y. Xu, E. R. Sanchez, J. C. Samson, G. D. Reeves, J. M. Ruohoniemi, and J. B. Sigwarth (2002), Auroral poleward boundary intensifications and tail bursty flows: A manifestation of a large-scale ULF oscillation?, *J. Geophys. Res.*, *107*(A11), 1352, doi:10.1029/2001JA000242.

Mauk, B. H., and C. I. Meng (1983), Characterization of geostationary particle signatures based on the 'injection boundary' model, *J. Geophys. Res.*, *88*, 3055–3071, doi:10.1029/JA088iA04p03055.

McComas, D. J., S. J. Bame, P. Barker, W. C. Feldman, J. L. Phillips, P. Riley, and J. W. Griffee (1998), Solar Wind Electron Proton Alpha Monitor (SWEPAM) for the Advanced Composition Explorer, *Space Sci. Rev.*, *86*, 563–612, doi:10.1023/A:1005040232597.

McIlwain, C. E. (1974), Substorm injection boundaries, in *Magnetospheric Physics*, vol. 43, edited by B. M. McCormac, p. 143, D. Reidel, Norwell, Mass.

McPherron, R. L. (1970), Growth phase of magnetospheric substorms, *J. Geophys. Res.*, *75*, 5592–5599, doi:10.1029/JA075i028p05592.

McPherron, R. L., and T. S. Hsu (2002), A comparison of substorms occurring during magnetic storms with those occurring during quiet times, *J. Geophys. Res.*, *107*(A9), 1259, doi:10.1029/2001JA002008.

McPherron, R. L., C. T. Russell, and M. P. Aubry (1973), Satellite studies of magnetospheric substorms on August 15, 1968: 9. Phenomenological model for substorms, *J. Geophys. Res.*, *78*, 3131–3149, doi:10.1029/JA078i016p03131.

McPherron, R. L., J. M. Weygand, and T. S. Hsu (2008), Response of the Earth's magnetosphere to changes in the solar wind, *J. Atmos. Solar Terr. Phys.*, *70*, 303–315, doi:10.1016/j.jastp.2007.08.040.

Mende, S. B. et al. (2000a), Far ultraviolet imaging from the IMAGE spacecraft: 1. System design, *Space Sci. Rev.*, *91*, 243–270.

Mende, S. B., et al. (2000b), Far ultraviolet imaging from the IMAGE spacecraft: 2. Wideband FUV imaging, *Space Sci. Rev.*, *91*, 271–285.

Milan, S. E., M. Lester, S. W. H. Cowley, K. Oksavik, M. Brittnacher, R. A. Greenwald, G. Sofko, and J. P. Villain (2003), Variations in the polar cap area during two substorm cycles, *Ann. Geophys.*, *21*, 1121–1140.

Milan, S. E., J. A. Wild, B. Hubert, C. M. Carr, E. A. Lucek, J. M. Bosqued, J. F. Watermann, and J. A. Slavin (2006), Flux closure during a substorm observed by Cluster, Double Star, IMAGE FUV, SuperDARN, and Greenland magnetometers, *Ann. Geophys.*, *24*, 751–767.

Milan, S. E., G. Provan, and B. Hubert (2007), Magnetic flux transport in the Dungey cycle: A survey of dayside and nightside reconnection rates, *J. Geophys. Res.*, *112*, A01209, doi:10.1029/2006JA011642.

Milan, S. E., P. D. Boakes, and B. Hubert (2008), Response of the expanding/contracting polar cap to weak and strong solar wind driving: Implications for substorm onset, *J. Geophys. Res.*, *113*, A09215, doi:10.1029/2008JA013340.

Milan, S. E., A. Grocott, C. Forsyth, S. M. Imber, P. D. Boakes, and B. Hubert (2009a), A superposed epoch analysis of auroral evolution during substorm growth, onset and recovery: open magnetic flux control of substorm intensity, *Ann. Geophys.*, *27*, 659–668.

Milan, S. E., J. Hutchinson, P. D. Boakes, and B. Hubert (2009b), Influences on the radius of the auroral oval, *Ann. Geophys.*, *27*, 2913–2924.

Miyashita, Y., Y. Kamide, S. Machida, K. Liou, T. Mukai, Y. Saito, A. Ieda, C. I. Meng, and G. K. Parks (2004), Difference in magnetotail variations between intense and weak substorms, *J. Geophys. Res.*, *109*, A11205, doi:10.1029/2004JA010588.

Morley, S. K., and M. P. Freeman (2007), On the association between northward turnings of the interplanetary magnetic field and substorm onsets, *Geophys. Res. Lett.*, *34*, L08104, doi:10.1029/2006GL028891.

Nagai, T., M. Fujimoto, R. Nakamura, W. Baumjohann, A. Ieda, I. Shinohara, S. Machida, Y. Saito, and T. Mukai (2005), Solar wind control of the radial distance of the magnetic reconnection site in the magnetotail, *J. Geophys. Res.*, *110*, A09208, doi:10.1029/2005JA011207.

Nishida, A., K. Uesugi, I. Nakatani, T. Mukai, D. H. Fairfield, and M. H. Acuna (1992), Geotail mission to explore earth's magnetotail, *Eos Trans. AGU*, *73*, 425, doi:10.1029/91EO00314.

Ogilvie, K. W., et al. (1995), SWE, a comprehensive plasma instrument for the Wind spacecraft, *Space Sci. Rev.*, *71*, 55–77, doi:10.1007/BF00751326.

Perreault, P., and S. I. Akasofu (1978), Study of geomagnetic storms, *Geophys. J. Roy. Astron. Soc.*, *54*, 547–573, doi:10.1111/j.1365-246X.1978.tb05494.x.

Reeves, G. D., M. G. Henderson, P. S. McLachlan, R. D. Belian, R. H. W. Friedel, and A. Korth (1996), Radial propagation of substorm injections, in *Proceedings of ICS-3, Versailles, France, 12–17 May 1996*, *Eur. Space Agency Spec. Publ.*, *ESA SP-389*, 579–584.

Sarris, T., and X. Li (2005), Evolution of the dispersionless injection boundary associated with substorms, *Ann. Geophys.*, *23*, 877–884.

Smith, C. W., J. L'Heureux, N. F. Ness, M. H. Acuna, L. F. Burlaga, and J. Scheifele (1998), The ACE magnetic fields experiment, *Space Sci. Rev.*, *86*, 613–632, doi:10.1023/A:1005092216668.

Stone, E. C., A. M. Frandsen, R. A. Mewaldt, E. R. Christian, D. Margolies, J. F. Ormes, and F. Snow (1998), The Advanced Composition Explorer, *Space Sci. Rev.*, *86*, 1–22, doi:10.1023/A:1005082526237.

Weimer, D. R. (1994), Substorm time constants, *J. Geophys. Res.*, *99*, 11,005–11,015, doi:10.1029/93JA02721.

Weimer, D. R., D. M. Ober, N. C. Maynard, M. R. Collier, D. J. McComas, N. F. Ness, C. W. Smith, and J. Watermann (2003), Predicting interplanetary magnetic field (IMF) propagation delay times using the minimum variance technique, *J. Geophys. Res.*, *108*(A1), 1026, doi:10.1029/2002JA009405.

Yeoman, T. K., M. P. Freeman, G. D. Reeves, M. Lester, and D. Orr (1994), A comparison of midlatitude Pi 2 pulsations and geostationary orbit particle injections as substorm indicators, *J. Geophys. Res.*, *99*, 4085–4093, doi:10.1029/93JA03233.

Zesta, E., E. Donovan, L. Lyons, G. Enno, J. S. Murphree, and L. Cogger (2002), Two-dimensional structure of auroral poleward boundary intensifications, *J. Geophys. Res.*, *107*(A11), 1350, doi:10.1029/2001JA000260.

Zhou, X. Y., and B. T. Tsurutani (2001), Interplanetary shock triggering of nightside geomagnetic activity: Substorms, pseudobreakups, and quiescent events, *J. Geophys. Res.*, *106*, 18,957–18,967, doi:10.1029/2000JA003028.

G. A. Abel, G. Chisham, and M. P. Freeman, British Antarctic Survey, Madingley Road, Cambridge CB3 0ET, UK.

P. D. Boakes and S. E. Milan, Department of Physics and Astronomy, University of Leicester, University Road, Leicester LE1 7RH, UK. (p.boakes@ion.le.ac.uk)

B. Hubert, Laboratory of Planetary and Atmospheric Physics, University of Liège, B-4000 Liège, Belgium.